J. Fluid Mech. (1984), *vol.* 138, *pp.* 297–323
Printed in Great Britain

On the stability of the decelerating laminar boundary layer

By MOHAMED GAD-EL-HAK, STEPHEN H. DAVIS†, J. THOMAS McMURRAY AND STEVEN A. ORSZAG‡
Flow Research Company, 21414 68th Avenue South, Kent, Washington 98032

(Received 3 May 1983 and in revised form 21 September 1983)

The stability of a decelerating boundary-layer flow is investigated experimentally and numerically. Experimentally, a flat plate having a Blasius boundary layer is decelerated in an 18 m towing tank. The boundary layer becomes unstable to two-dimensional waves, which break down into three-dimensional patterns, hairpin vortices, and finally turbulent bursts when the vortices lift off the wall. The unsteady boundary-layer equations are solved numerically to generate instantaneous velocity profiles for a range of boundary and initial conditions. A quasi-steady approximation is invoked and the stability of local velocity profiles is determined by solving the Orr–Sommerfeld equation using Chebyshev matrix methods. Comparisons are made between the numerical predictions and the experimentally observed instabilities.

1. Introduction

The classical vehicle for studying shear-flow transition to turbulence consists of a uniform steady flow toward the leading edge of a fixed flat plate. Somewhat downstream of the leading edge a Blasius boundary layer develops. In various stages and in various sequences (to be detailed below) this Blasius layer undergoes small-amplitude instability, nonlinear development and transition to turbulence as the displacement-thickness Reynolds number R_{δ^*} increases (Klebanoff, Tidstrom & Sargent 1962). In effect, R_{δ^*} measures the distance from the leading edge of the plate.

Linearized stability theory can be applied to Blasius profiles treated as locally parallel flows (Lin 1955; Drazin & Reid 1981). Squire's (1933) theorem shows that two-dimensional travelling waves, Tollmien–Schlichting waves, are the most dangerous for instability and become unstable when R_{δ^*} exceeds about 520 for long waves having downstream wavenumber $\alpha^* = 0.30$ (Jordinson 1970). When the above Orr–Sommerfeld theory is modified to take account of non-parallel effects in the boundary layer, the critical R_{δ^*} is reduced to about 420 (Saric & Nayfeh 1975). However, as soon as nonlinear effects are allowed, three-dimensional disturbances can no longer be excluded.

Observations in experiments having 'natural' transition show that clean two-dimensional waves are rarely attainable; rather three-dimensional structure is immediately seen. Efforts to 'control' the disturbances have led to the introduction of vibrating ribbons (Klebanoff *et al.* 1962) oscillating in ostensibly two-dimensional motions. Although these ribbons are introduced to develop two-dimensional structure,

† Permanent address: Department of Engineering Science and Applied Mathematics, Northwestern University, Evanston, IL 60201.
‡ Permanent address: Department of Mathematics, Massachusetts Institute of Technology, Cambridge, MA 02139.

clear three-dimensional fluid motions are still seen. Longitudinal strips of tape have subsequently been introduced to at least fix the spatial structure of this three-dimensional flow (Klebanoff *et al.* 1962). Given the three-dimensional character of the flow, the road to transition involves amplification of the three-dimensionality, development of 'hairpin' vortices and finally the 'bursts' of turbulence.

The difficulty in the attainment of purely two-dimensional disturbances and the seeming simultaneous occurrence of both two- and three-dimensional waves has led to several recent attempts at wave-interaction theories (Craik 1971, 1980; Nayfeh & Bozatli 1979). Here Tollmien–Schlichting waves and oblique waves are sought that can lead, through weakly nonlinear interactions, to resonant-like behaviour that selects the observed structure prior to bursting. The selection of three-dimensional structure must thus overcome the higher growth rates (Squire's theorem) of the Tollmien–Schlichting waves. Each of these analyses models certain features of the early transition process, but not one is completely satisfactory.† Finally, there seems to be no theory that is yet capable of the prediction of the hairpin vortices, although there is substantial agreement that intensification of longitudinal vorticity gives rise to locally inflexional (unsteady and three-dimensional) velocity profiles (Stuart 1965). These profiles seemingly break down (Klebanoff *et al.* 1962), giving small (spatial) scale features associated with the burst.

An alternative vehicle for the study of the transition process is the decelerating-plate experiment (Fales 1955; Hegarty 1958; Davis & Gad-el-Hak 1981). Here a plate of length L moves steadily normal to its leading edge; L is short enough that the Blasius layer remains laminar along its full length. At time $t = 0$ the plate is decelerated from a constant initial speed U_0 to a new constant final speed U_∞. Flow visualization seemingly shows that a sequence of two-dimensional structures, three-dimensional structures, hairpin vortices and then turbulent bursts results. When the deceleration takes place, the *instantaneous* velocity profiles are inflexional. If the inviscid instability associated with the instantaneous inflexion point has large enough growth rate, then there is an instability which will cause two-dimensional waves to grow in the unsteady flow (Drazin & Reid 1981). Subsequently there is a breakdown (perhaps a new instability of the two-dimensional structure) into three dimensions, an intensification of the three-dimensional structure, the development of hairpin vortices and then turbulent bursts.

The deceleration experiment differs from the fixed-plate experiment in several respects. First, given the inflexional character of the initial instability, the two-dimensional waves would have substantially larger growth rates than their Tollmien–Schlichting counterparts (Drazin & Reid 1981). Hence there *may* develop a 'clean', strongly two-dimensional wave field during the initial stages of the transition process. This contrasts with the mixed two-dimensional–three-dimensional field for the fixed-plate experiment (Anders & Blackwelder 1979). Careful point measurements are required to determine whether this is the case. If this is the case, it suggests the study of this instability in order to determine the mechanism and characteristics of the development of three-dimensionality. The isolation of this problem is one of the main advantages of the deceleration experiment over the fixed-plate experiment. If this picture is correct and there is a well-defined transition from laminar two-dimensional waves to laminar three-dimensional waves through an instability process (Orszag & Patera 1983), one has identified a major link in the transition process. An understanding

† Orszag & Patera (1983) have shown that a pure two-dimensional structure is prone to strong three-dimensional instabilities.

of this instability allows one to contemplate means of interfering with the process to delay transition or reinforcing the process to foster transition. It gives one a handle in examining the subsequent *evolution to* hairpin vortices, since these might be examined through the nonlinear evolution of the three-dimensional structure. In summary, the deceleration experiment might be one that clearly separates two-dimensional structures from three-dimensional ones and allows analysis of the change from one to the other.

The present investigation was undertaken to address some of the questions raised above. Experimental and numerical investigations were carried out to determine the mechanics of transition on a decelerating flat plate. A flat plate was towed in the Flow Research 18 m towing tank. Visualization and probe measurement techniques were used to study the different instabilities resulting from decelerating the plate. The unsteady boundary-layer equations were solved numerically to generate instantaneous velocity profiles for a range of boundary and initial conditions. The stability of such profiles was determined by solving the Orr–Sommerfeld equations using Chebyshev matrix methods.

2. Experimental equipment and procedure

2.1. *Towing-tank system*

The 18 m long, 1.2 m wide and 0.9 m deep towing tank and associated equipment have been described by Gad-el-Hak, Blackwelder & Riley (1981). The flat plate was rigidly mounted under a carriage that rides on two tracks mounted on top of the towing tank. During towing, the carriage was supported by an oil film which insured a vibrationless tow, so that the flow field had an equivalent freestream turbulence of about 0.1 %. The carriage was towed with two cables driven through a reduction gear by a 1.5 h.p. Boston Ratiotrol motor. The towing speed was regulated within an accuracy of 0.1 %. The main frame supporting the tank could be tilted and levelled by adjusting four screw jacks. This feature was essential for smooth operation of the carriage, whose tracks are supported by the main frame. The towing tank was designed so that flow visualization can be made from the top, sides, bottom and ends. The bottom and sidewalls are made of 19 mm thick plate glass with optical quality. The endwalls are made of 38 mm thick Plexiglas.

2.2. *Model and test conditions*

A modularly designed flat plate was built for the present experiment. Figure 1 is a schematic of the plate, which is 2.7 m long and 1.1 m wide. The working surface is made of Plexiglas and contains two dye slots, each with four separate compartments. The working surface is placed on a sheet of 6 mm Plexiglas that is bonded to a 13 mm honeycomb. The NOMEX honeycomb, covered on the bottom side with fibreglass resin, provides buoyancy as well as bending strength. A system of cables and pulleys on the bottom surface insures the flatness of the working surface to within 0.2 mm.

Separation and premature transition at the leading edge is prevented by using a 12:1 elliptic nose and an adjustable lifting flap at the trailing edge. In the range of towing speeds of 20–60 cm/s, a Blasius laminar boundary layer is generated on the working surface.

Uniform deceleration was attained by decreasing the voltage to the Ratiotrol motor. The initial and final speeds were changed in the range of 60–0 cm/s and the deceleration rate varied in the range 1–60 cm/s^2.

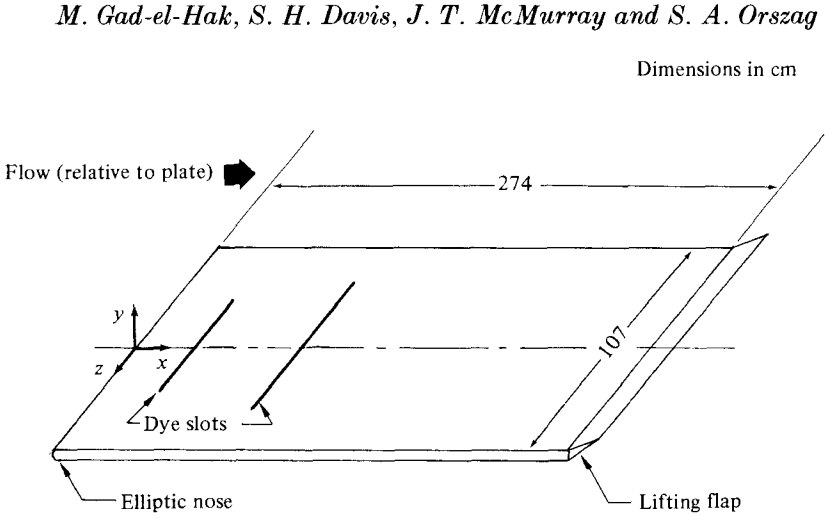

FIGURE 1. Schematic of the flat plate and coordinate system.

2.3. *Flow visualization*

The transition events were made visible by novel techniques which utilized fluorescent dye, i.e. dye which is visible only when excited by a strong light source of the appropriate wavelength (Gad-el-Hak, Blackwelder & Riley 1979). This provided an extra degree of freedom in observing the flow because both the dye and light location could be controlled. A 5 W argon laser (Spectra Physics, Model 164) was used with a cylindrical lens to produce a sheet of light that could be projected perpendicular to each of the three axes as required. The light sheets were approximately 1 mm thick, which was sufficient to resolve the large structure within the transitional and turbulent regions.

Two different methods of dye injection were employed. In the first, a dye sheet seeped into the laminar boundary layer through either of two 0.15 mm wide, 30 cm long spanwise slots located 40 cm and 75 cm downstream of the leading edge. The slots were milled at a 45° angle inclined towards the trailing edge to minimize flow disturbance. Each slot was divided into four separate sections, each with its own dye source, so the spanwise mixing and diffusion of turbulent fluid could be studied. The dye remained on the plate surface until an upward motion caused it to lift. In the second, discrete lines of dye could be allowed to seep into the laminar boundary layer by masking the spanwise slot with a 32 cm long strip of electrical tape, in which thirty longitudinal slots, 1 cm apart and 0.5 cm long, were cut with a surgical knife. The resulting dyelines were less than 0.5 mm wide near the trailing edge of the plate.

2.4. *Hot-film probes*

Miniature hot-film probes (Thermo Systems Inc., Model 1260) were used in the present investigation to measure the instantaneous longitudinal velocity before, during and after deceleration. The probe diameter was 0.025 mm and its sensing length was 0.25 mm. The probe support was 0.9 mm diameter and 32 mm long. To obtain a velocity profile, a five-probe traverse powered with a stepping motor controlled through an Apple-II microcomputer was used. For data acquisition and analyses, NOVA 800 and Prime 750 minicomputers were used.

3. Analyses

3.1. *Theoretical considerations*

3.1.1. *Basic state: the unsteady boundary layer*

The flow that initially becomes unstable is an unsteady boundary layer caused by plate deceleration. The initial and final states are Blasius layers. Hence one must solve (Rosenhead 1963; Schlichting 1968)

$$\psi_{yt}+\psi_y\psi_{xy}-\psi_x\psi_{yy}=\psi_{yyy}, \tag{1a}$$

$$\psi(x,\infty,t)=0 \quad (0<x<1, \quad t\geqslant 0), \tag{1b}$$

$$\psi_x(x,0,t)=0 \quad (0<x<1, \quad t\geqslant 0), \tag{1c}$$

$$\psi_y(x,0,t)=-\frac{U_w(t)}{U_0} \quad (0<x<1, \quad t\geqslant 0), \tag{1d}$$

$$\psi(x,y,t)=\psi_B(x,y) \quad (0<x<1, \quad t<0, \quad y\geqslant 0). \tag{1e}$$

Equation (1*a*) is the non-dimensional longitudinal momentum equation, with the familiar boundary-layer approximations applied. In this equation the downstream coordinate x is non-dimensionalized by L, the normal coordinate y by $L/R^{\frac{1}{2}}$, the time t by L/U_0, and the stream function ψ by $U_0 L/R^{\frac{1}{2}}$, where the Reynolds number $R\equiv U_0 L/\nu$. Here $U_w(t)$ is the speed history of the plate, ψ_B signifies the stream function of the Blasius solution *prior* to deceleration. The unsteady term in (1*a*) makes the boundary layer non-similar.

The unsteady boundary-layer solution of system (1)

$$\psi=\psi(x,y,t) \tag{2}$$

is of a combined Blasius–Rayleigh type (Stewartson 1951).

3.1.2. *Linear stability analysis for locally parallel flow*

The onset of shear instabilities is obtained by linear stability analysis of the flow (2). Here ψ is unsteady, but we shall only examine the 'quasi-steady' stability problem in which the instantaneous profiles

$$\psi_s=\psi_s(x,y;t_0)\equiv\psi(x,y,t=t_0) \tag{3}$$

are treated as steady parallel flows with the Orr–Sommerfeld equation. Such an approximation is valid if the time rate of change of ψ (measured by a viscous diffusion time) is slow compared with the rate of growth of disturbances of ψ_s (measured by a convection time). The validity of this approximation will be discussed at the end of §4.3. The following Orr–Sommerfeld system defines a critical value of R_{δ^*} for each profile (parameterized by t_0):

$$(\mathrm{D}^2-\alpha^2)^2\phi=\mathrm{i}\bar{R}\left[(\alpha U(y)-\omega)(\mathrm{D}^2-\alpha^2)\phi-\alpha\frac{\mathrm{d}^2U}{\mathrm{d}y^2}\phi\right], \tag{4a}$$

$$\phi(0)=0, \tag{4b}$$

$$\mathrm{D}\phi(0)=0, \tag{4c}$$

$$\phi(\infty)=0, \tag{4d}$$

where we have written the normal modes as follows:

$$\psi(x,y,t)=\phi(y)\,\mathrm{e}^{\mathrm{i}(\alpha x-\omega t)}. \tag{5}$$

Here α is the downstream wavenumber and ω is the complex frequency; $\mathrm{D} \equiv \mathrm{d}/\mathrm{d}y$, and $\bar{R}$ is related to the standard displacement-thickness Reynolds number R_{δ^*} by

$$\bar{R} = R^{\frac{1}{2}} = \left(\frac{U_0 L}{\nu}\right)^{\frac{1}{2}}, \tag{6}$$

$$R_{\delta^*} = \bar{R}^2 \frac{U_w}{U_0} \frac{\delta^*}{L}. \tag{7}$$

Given that we have used the quasi-steady assumption, Squire's theorem applies and allows us to confine our attention to two-dimensional disturbances only. This is reflected in the form (5).

There is a 'most-dangerous' profile that corresponds to $t_0 = t_{0c}$; where t_{0c} is a measure of the time delay between deceleration and the appearance of the first two-dimensional instability. Presumably the instability is due to the inflexional nature of the profile. Here the point of inflexion at $t = 0$ is at the wall and moves outward on a diffusion timescale. Its location is $y = y_{IP}$; if y_{IP} is too small, viscous effects stabilize the profile. If y_{IP} is too large, the inflexion point is in a region where U is very small, so the instability is not important. The 'most-dangerous' profile corresponds to an intermediate value of y_{IP} and hence of t_0.

3.2. *Numerical methods*

A code was developed to solve the unsteady boundary-layer equation (1) as follows. First, the flow variables are expanded in mapped Chebyshev polynomial expansions. Thus the variable y is mapped to a new variable Z using

$$y = S_1 \frac{1+Z}{S_2 - Z} \quad (-1 \leqslant Z < 1), \tag{8}$$

where S_1 and S_2 are suitable scale parameters. In terms of Z, y-derivatives take the form:

$$\frac{\partial F}{\partial y} = \frac{(S_2 - Z)^2}{S_1(1+S_2)} \frac{\partial F}{\partial Z}. \tag{9}$$

Secondly, the various functions are expanded in Chebyshev-polynomial series in Z:

$$F(Z) = \sum_{n=0}^{N} f_n T_n(Z). \tag{10}$$

Here the nth Chebyshev polynomial $T_n(Z)$ is defined by

$$T_n(Z) = \cos(n \arccos Z), \tag{11}$$

for all non-negative integers n (see e.g. Fox & Parker 1968). Some examples are $T_0(Z) = 1$, $T_1(Z) = Z$, $T_2(Z) = 2Z^2 - 1$. Also, if $F(Z)$ is represented as in (10), then

$$F'(Z) = \sum_{n=0}^{N} f_n^{(1)} T_n(Z), \tag{12}$$

with

$$f_{n-1}^{(1)} - f_{n+1}^{(1)} = 2n f_n \quad (n > 1). \tag{13}$$

Thirdly, the boundary-layer equation is solved by discretizing x and t using Crank–Nicolson implicit space and time differencing, in which the difference approximations

$$\left(\frac{\partial F}{\partial t}\right)_{(k+\frac{1}{2})\,\Delta t} = \frac{F[(k+1)\,\Delta t] - F(k\Delta t)}{\Delta t}, \tag{14}$$

$$\left(\frac{\partial F}{\partial x}\right)_{(j+\frac{1}{2})\,\Delta x} = \frac{F[(j+1)\,\Delta x] - F(j\Delta x)}{\Delta x} \tag{15}$$

are used. At the centred points $(j+\frac{1}{2})\,\Delta x$ and $(k+\frac{1}{2})\,\Delta t$, these difference approximations are second-order accurate in both x and t. The fact that (14) and (15) involve functions at the discrete points $(j+1)\,\Delta x$ and $(k+1)\,\Delta t$ implies that implicit equations must be solved for the dependent variables. These implicit equations are set up using the Chebyshev derivative matrix operator D defined by

$$F'(Z_j) = \sum_{n=0}^{N} (\mathrm{D}f)_n \, T_n(Z_j), \tag{16}$$

where Z_j are the Chebyshev collocation points:

$$Z_j = \cos\frac{\pi j}{N}. \tag{17}$$

The resulting equation for the stream function is nonlinear. This nonlinear equation is solved by quasi-linearization (Newton's method). The resulting iterative scheme is expressible in terms of the operator (matrix) C, defined by

$$\begin{aligned}\mathrm{C} \equiv \frac{1}{2\Delta t}\mathrm{D} - \frac{1}{2\Delta x}[\Psi_y^{(q)}(x_j, t_{k+1})\,\mathrm{D} + \tfrac{1}{4}\{\Psi(x_{j+1}, t_k) \\ + \Psi(x_{j+1}, t_{k+1}) - \Psi(x_j, t_k) - \Psi^{(q)}(x_j, t_{k+1})\}\,\mathrm{D}^2] - \tfrac{1}{4}\mathrm{D}^3 \\ + \frac{1}{8\Delta x}[\Psi_{yy}(x_j, t_k) + \Psi_{yy}(x_{j+1}, t_k) + \Psi_{yy}(x_{j+1}, t_{k+1}) + \Psi_{yy}^{(q)}(x_j, t_{k+1})],\end{aligned} \tag{18}$$

as

$$\begin{aligned}&\mathrm{C}\{\Psi^{(q+1)}(x_j, t_{k+1}) - \Psi^{(q)}(x_j, t_{k+1})\} \\ &= -\Big\{[\Psi_y^{(q)}(x_j, t_{k+1}) + \Psi_y(x_{j+1}, t_{k+1}) - \Psi_y(x_j, t_k) - \Psi_y(x_{j+1}, t_k)]\frac{1}{2\Delta t} \\ &\quad + [\Psi_y(x_{j+1}, t_k)^2 + \Psi_y(x_{j+1}, t_{k+1})^2 - \Psi_y(x_j, t_k)^2 - \Psi_y^{(q)}(x_j, t_{k+1})^2 \\ &\quad - \tfrac{1}{2}(\Psi(x_{j+1}, t_k) + \Psi(x_{j+1}, t_{k+1}) - \Psi(x_j, t_k) - \Psi^{(q)}(x_j, t_{k+1})) \\ &\quad \times (\Psi_{yy}(x_{j+1}, t_k) + \Psi_{yy}(x_j, t_k) + \Psi_{yy}(x_{j+1}, t_{k+1}) + \Psi_{yy}^{(q)}(x_j, t_{k+1}))]\frac{1}{4\Delta x} \\ &\quad + \Psi_{yyy}^{(q)}(x_j, t_{k+1}) - \tfrac{1}{4}(\Psi_{yyy}(x_{j+1}, t_k) + \Psi_{yyy}(x_j, t_k) + \Psi_{yyy} \\ &\qquad + (x_{j+1}, t_{k+1}) + \Psi_{yyy}^{(q)}(x_j, t_{k+1}))\Big\}.\end{aligned} \tag{19}$$

Here $\Psi(x, t)$ is the converged value of $\Psi^{(q)}(x, t)$ at each discrete point (x_j, t_k). Typically, only a few iterations are necessary to converge. The advantage of this method is that it is unconditionally stable.

At the inflow location x_0 Blasius flow is imposed. The Blasius equation is solved by the Chebyshev spectral scheme outlined above, also using Newton's method.

At each downstream location, the flow field can be subjected to stability analysis using the Orr–Sommerfeld equation applied to the instantaneous velocity profile. The Orr–Sommerfeld system (4) is solved using Chebyshev-polynomial spectral methods on the same Z_j grid described above. The Chebyshev approximations permit simulations of very high accuracy. The Orr–Sommerfeld eigenvalue problem for temporally unstable mode is formulated as a generalized matrix eigenvalue problem of the form

$$\boldsymbol{A\Phi} = \lambda \boldsymbol{B\Phi}. \tag{20}$$

The eigenvalues of the resulting matrix problem are found by first reducing the problem (20) (with a singular matrix $\boldsymbol{B}$) to a standard eigenvalue problem of the form $\boldsymbol{Ax} = \lambda \boldsymbol{x}$ with scalar λ and then finding the eigenvalues of this problem using the QR

method (Orszag 1971). If a good guess for an eigenvalue is available, then the code is able to avoid the global QR computation by using a local inverse Rayleigh iteration method to improve the guess. In all cases, the matrix method is designed so that the only unstable modes that are computed (either globally or locally) are approximations to physical modes; there are no spurious unstable modes. This feature is achieved by writing Orr–Sommerfeld equation in such a form that the numerical method would give a stable forward time-integration method for the linearized Navier–Stokes equations, so spurious unstable modes (that would lead to numerical instability in time) cannot be present.

The code also has the optional features of obtaining the minimum critical Reynolds number at a given x-station and the neutral curve at the given x-station. These computations are done using variants of Newton's method. Thus quick convergence of a guess to the neutral curve $\operatorname{Im}\omega = 0$ is obtained by the iterative method:

$$\omega = \omega(\alpha_n, \bar{R}_n), \tag{21}$$

$$\alpha_{n+1} = \alpha_n - \frac{(\operatorname{Im}\omega)\dfrac{\partial \operatorname{Im}\omega}{\partial\alpha}}{\left(\dfrac{\partial \operatorname{Im}\omega}{\partial\alpha}\right)^2 + \left(\dfrac{\partial \operatorname{Im}\omega}{\partial\bar{R}}\right)^2}, \tag{22}$$

$$\bar{R}_{n+1} = \bar{R}_n - \frac{(\operatorname{Im}\omega)\dfrac{\partial \operatorname{Im}\omega}{\partial\bar{R}}}{\left(\dfrac{\partial \operatorname{Im}\omega}{\partial\alpha}\right)^2 + \left(\dfrac{\partial \operatorname{Im}\omega}{\partial\bar{R}}\right)^2}. \tag{23}$$

Once one point on the neutral curve is obtained, additional points on it are obtained by using as a first guess a point of the form:

$$\hat{\alpha} = \alpha + q\frac{\partial}{\partial\bar{R}}\operatorname{Im}\omega, \tag{24}$$

$$\hat{\bar{R}} = \bar{R} - q\frac{\partial}{\partial\alpha}\operatorname{Im}\omega, \tag{25}$$

which is obtained by moving along the tangent to the neutral curve at the computed point.

The minimum-critical-Reynolds-number program also uses Newton's method. Here the iterative equations are

$$\alpha_{n+1} = \alpha_n + \Delta\alpha, \tag{26}$$

$$\bar{R}_{n+1} = \bar{R}_n + \Delta R, \tag{27}$$

$$\operatorname{Im}\omega(\alpha_n, \bar{R}_n) + \frac{\partial}{\partial\alpha}\operatorname{Im}\omega(\alpha_n, \bar{R}_n)\,\Delta\alpha + \frac{\partial}{\partial\bar{R}}\operatorname{Im}\omega(\alpha_n, \bar{R}_n)\,\Delta R = 0, \tag{28}$$

$$\frac{\partial}{\partial\alpha}\operatorname{Im}\omega(\alpha_n, \bar{R}_n) + \frac{\partial}{\partial\alpha^2}\operatorname{Im}\omega(\alpha_n, \bar{R}_n)\,\Delta\alpha + \frac{\partial^2}{\partial\alpha\,\partial\bar{R}}\operatorname{Im}\omega(\alpha_n, \bar{R}_n)\,\Delta R = 0. \tag{29}$$

In summary, the above-described code uses an unconditionally stable, spectral, accurate integration program for the solution of the time-dependent non-self-similar boundary-layer equations and both global and local spectral methods for the solution of the Orr–Sommerfeld equation. The code is reasonably robust, having significant difficulty only in cases when the flow reverses.

4. Results and discussion

4.1. *Flow-visualization results*

When the Blasius boundary layer was subjected to a uniform deceleration, a most interesting series of events was observed. Figure 2 represents six selected frames from a ciné film of the observed instabilities. The left-hand side of each frame was at $x = 92$ cm and the right-hand side was at $x = 108$ cm. Fluorescent dye seeped into the laminar boundary layer through the spanwise slot, and was illuminated by a horizontal sheet of laser light at $y = 0$. The thickness of the laser sheet was about 1 mm, several times the thickness of the undisturbed dye sheet. At a uniform speed of 40 cm/s the boundary layer was of Blasius type (see §4.2), and the dye sheet appeared smooth and uniform, as shown in figure 2(*a*). The plate was then decelerated uniformly to a speed 30 cm/s in 5 s. Two seconds after the deceleration had started, the two-dimensional pattern depicted on figure 2(*b*) was evident. The alternating bright and dark bands are consistent with the passing of two-dimensional vorticity waves. The wavelength of the disturbance was about 5–6 boundary-layer thicknesses δ as compared with a wavelength 8δ for a Tollmien–Schlichting wave occurring in a non-decelerating Blasius boundary layer having the same Reynolds number. The wave phase speed relative to the plate was about 10 cm/s as compared with 14 cm/s for the corresponding Tollmien–Schlichting wave. The two-dimensional waves developed a three-dimensional pattern as shown on figure 2(*c*). This pattern evolved into several hairpin vortices characterized by the bright triangles in figure 2(*d*).† Since the thickness of the sheet of light is larger than the thickness of the undisturbed dye, bright regions indicate lifting and accumulation of dye. The vortices appeared in several regular rows with a spanwise distance between two vortices of about 5δ (or about the same as the wavelength of the two-dimensional waves). The patterns continued to convect towards the trailing edge of the plate, and new ones appeared near the leading edge. Sideviews of the hairpin vortices indicated that their heads moved away from the wall. When the vortex head reached a height of about half a boundary-layer thickness it then burst into turbulence, as shown in figure 2(*e*). The turbulent regions grew in size, as shown in figure 2(*f*), and adjacent bursts coalesced. Shortly afterward the dye pattern indicated that the flow over the entire plate was turbulent.

The experiments were repeated with different initial velocities in the range 20–60 cm/s and different deceleration rates in the range 1–60 cm/s^2. The same sequence of events described above was observed in all runs. The lengthscales were not sensitive to the changes in the deceleration rate. However, the time to complete the transition process was approximately inversely proportional to the deceleration rate. The stages of transition are summarized in the schematic depicted in figure 3.

To gain more physical insight into the transition process in the decelerating boundary layer, the above-described sequence of events was also observed using discrete lines of dye embedded into the laminar boundary layer (§2.3). Figure 4 shows six selected frames from a ciné film of a typical run. Before decelerating the flat plate, the dyestreaks were parallel to the flow and remained on the plate surface. The plate was then decelerated from a speed 40 cm/s to a speed 30 cm/s in 5 s. A short time after the deceleration had started, the two-dimensional waves with their fronts perpendicular to the dye streaks appeared as alternating bright and dark bands on each streak as shown in figure 4(*a*). The waves moved in the same direction, relative

† Similar patterns were observed in the vibrating trip-wire experiments conducted by Perry, Lim & Teh (1981).

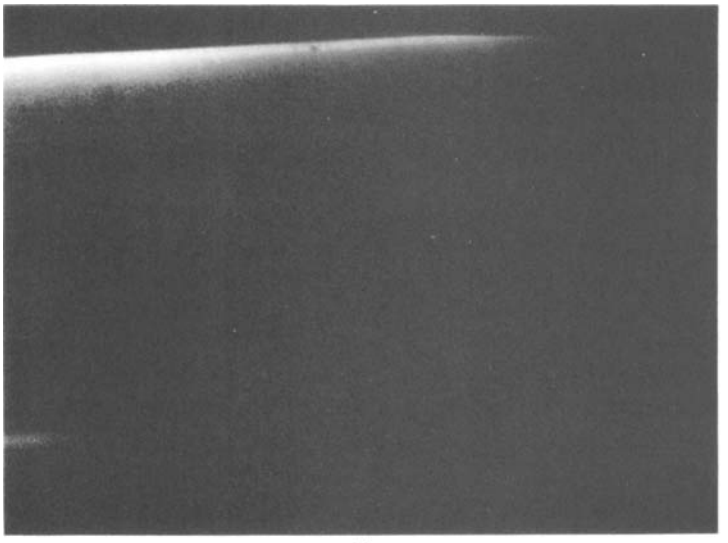

(a)

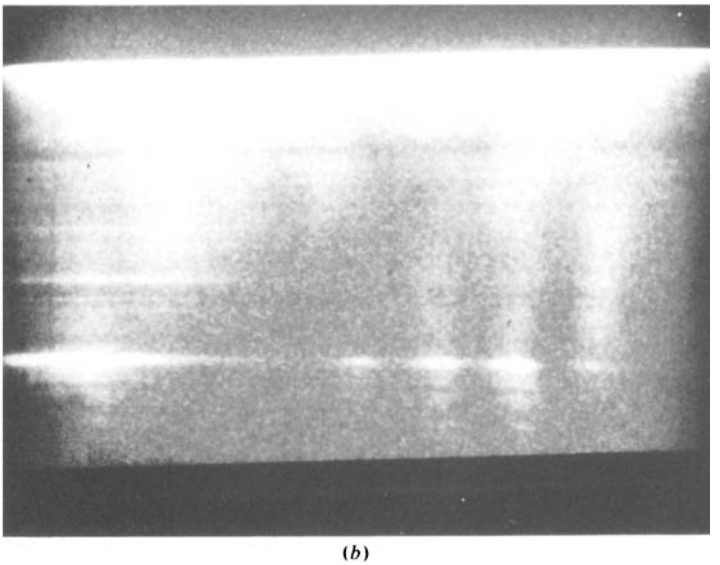

(b)

FIGURE 2(a, b). For caption see p. 308.

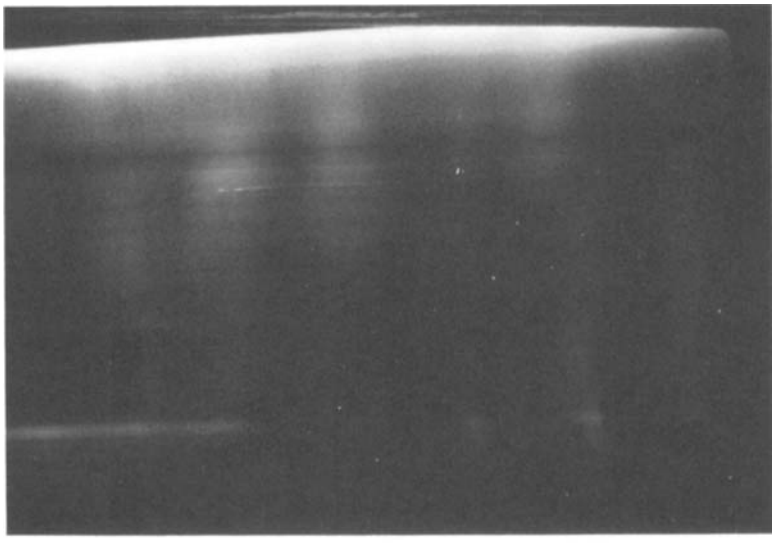

(*c*)

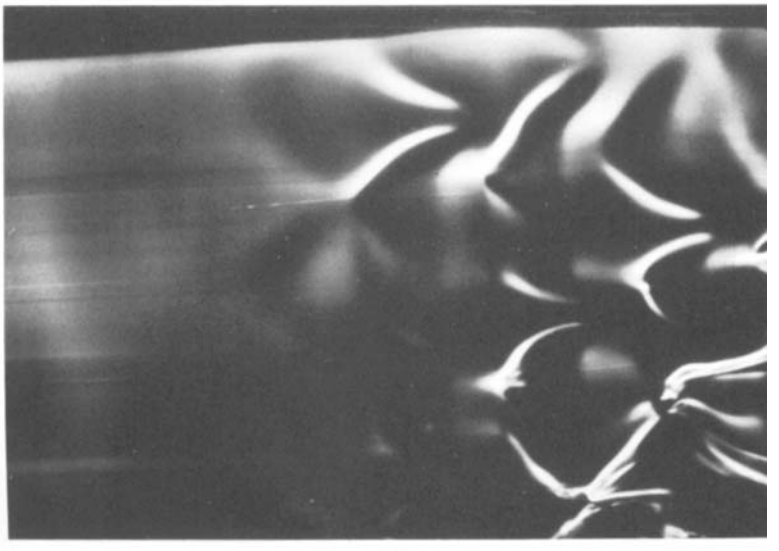

(*d*)

FIGURE 2(*c*, *d*). For caption see p. 308.

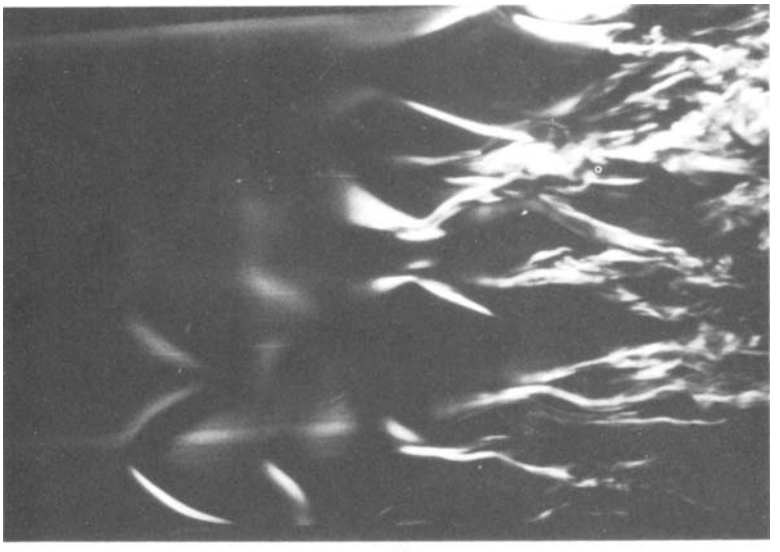

(e)

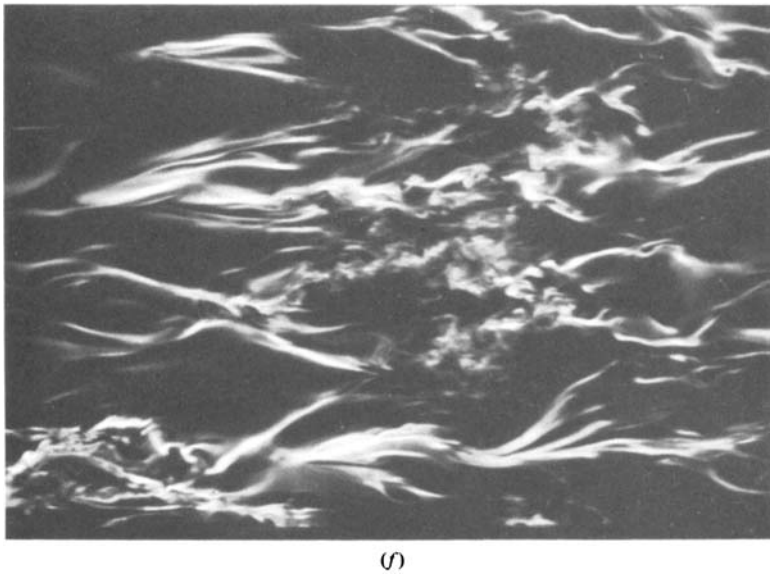

(f)

FIGURE 2. Instabilities in a decelerating boundary layer.

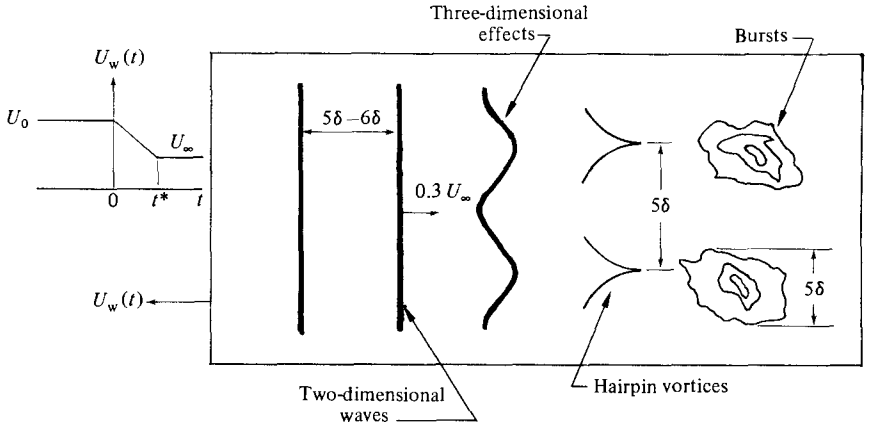

FIGURE 3. Schematic of transition events in a decelerating boundary layer.

to the plate, as the ambient fluid. As the amplitude of these two-dimensional waves increased, as evident by the intensification of the contrast between the bright and dark bands, three-dimensionality developed, the dyelines began to show a waviness that has the same wavelength as that of the original two-dimensional waves (figures 4*b*, *c*). Liepmann, Brown & Nosenchuck (1982), in observing a somewhat similar transition process initiated by a dynamic-heating technique, speculated that the waviness of the dyelines indicates a local development of longitudinal vorticity corresponding to the local warping of the initially parallel vortex lines. The dye became concentrated in regions that has been lifted away from the wall into a higher-velocity region of the boundary layer, thereby catching up with that released at an earlier time. The transition process continued as before until the dye pattern indicated turbulent flow over the entire plate (figures 4*d*–*f*).

4.2. *Hot-film-probe measurements*

Miniature hot-film probes were used to measure the instantaneous longitudinal velocity in the decelerating boundary layer. The probes were moved with the plate, so that all velocities recorded were relative to the plate. Before the deceleration started, the boundary layer was of Blasius type, as shown on figure 5. The velocity profiles are plotted in the normal boundary-layer coordinates, where the ambient speed U_0 is used as a velocity scale and the lengthscale $(\nu x/U_0)^{\frac{1}{2}}$ is proportional to the laminar boundary-layer thickness δ. The Reynolds number for the two runs shown on figure 5 was $U_0 x/\nu = 6.7 \times 10^5$ ($R_{\delta^*} = 1400$). The solid line in the figure is a numerically generated Blasius profile.

Figure 6 represents the instantaneous longitudinal velocity $U(y)$ at $y/\delta = 0.1$, for a plate decelerated from an initial velocity $U_0 = 40$ cm/s to a final velocity $U_\infty = 32$ cm/s in a time $t^* = 4.6$ s. The two arrows on the abscissa represent the starting and ending of deceleration. Initially, the flow is laminar and the velocity at this particular elevation is proportional to the towing speed. A short time† after the deceleration starts, a sinusoidal instability is observed. Its peak-to-peak amplitude grows rapidly as shown in figure 6. Characteristic turbulent fluctuations are then observed, followed by a return to the laminar state. This occurs about 8 s after the plate has moved at its new constant towing speed. The turbulence, on the average,

† The exact delay time between the start of deceleration and the onset of instability is difficult to determine, since the observed waves are infinitesimal at first.

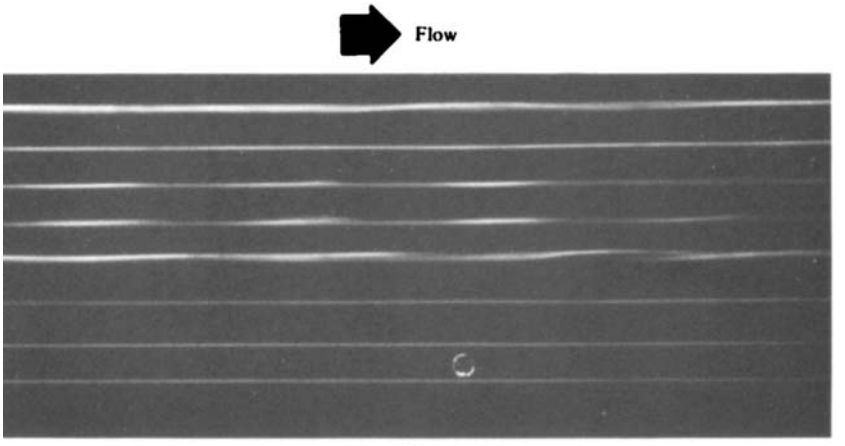

(a)

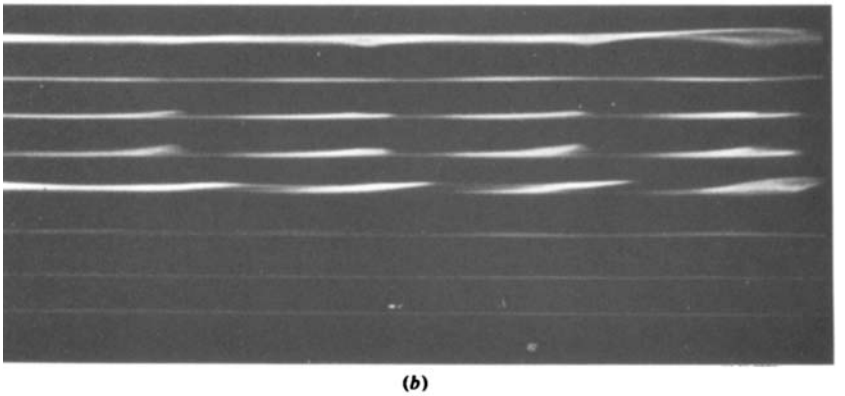

(b)

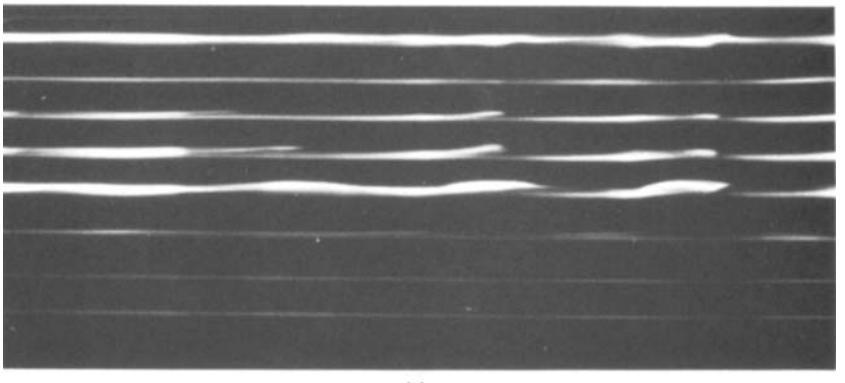

(c)

FIGURE 4 (*a–c*). For caption see facing page.

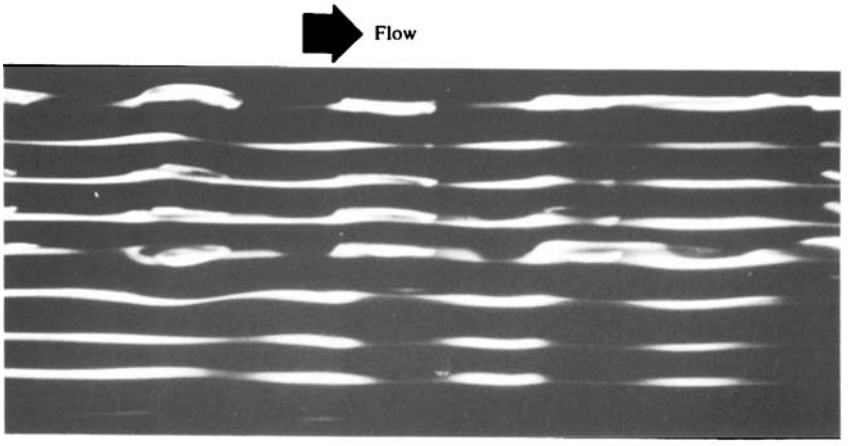

(*d*)

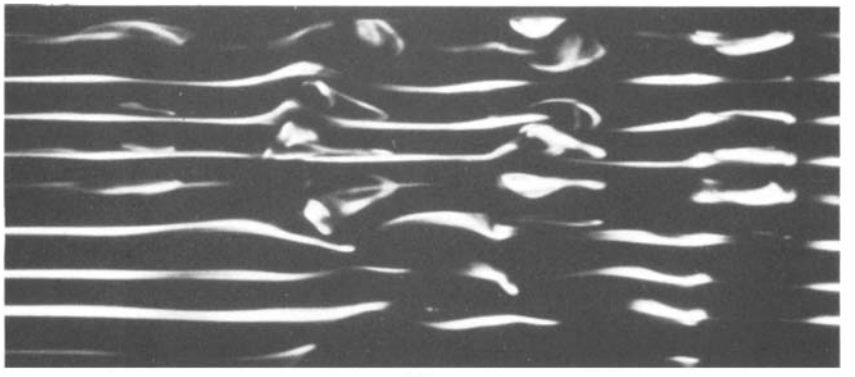

(*e*)

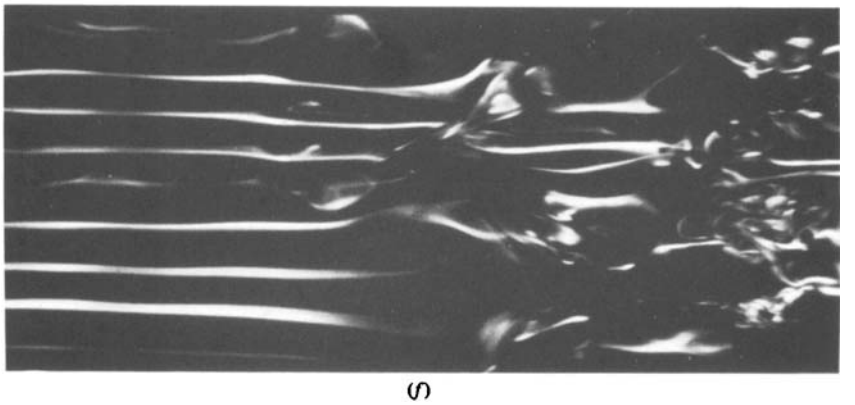

(*f*)

FIGURE 4. Dyestreak visualization during deceleration.

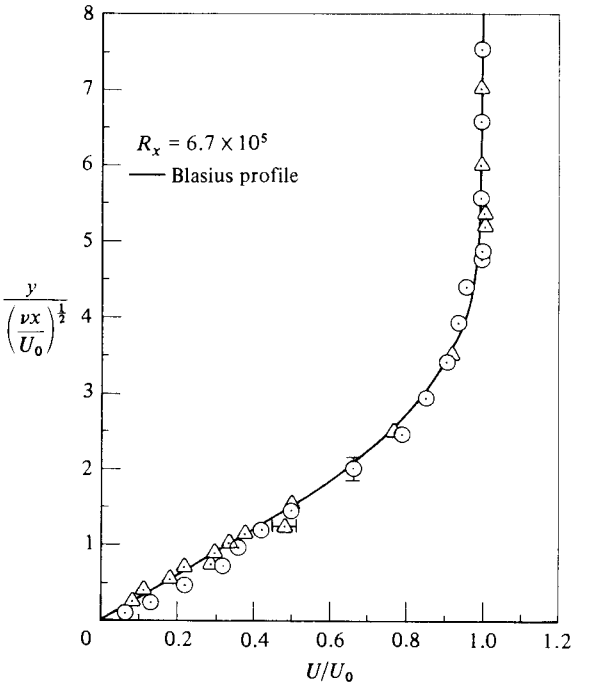

FIGURE 5. Laminar-boundary-layer profiles.

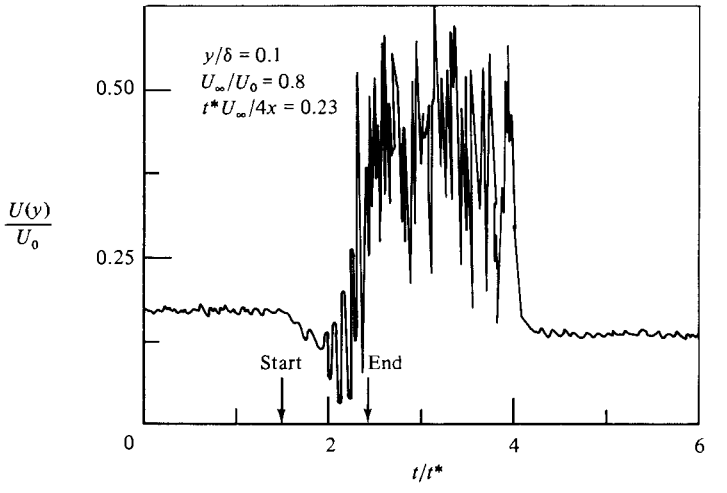

FIGURE 6. Longitudinal velocity near the wall.

brings high-speed fluid from outside the boundary layer to replace the low-speed fluid near the wall. A second probe at $y/\delta = 1$ recorded the signal shown in figure 7. It is seen that the turbulent fluctuations, on the average, bring low-speed fluid from the wall region to replace the high-speed fluid at $y/\delta = 1$. Close inspection of the instability waves near the wall and away from the wall reveals that the two wavetrains are out of phase, consistent with a spanwise vortical motion.

The instability waves appeared from the visualization experiments to be two-dimensional initially. To check the 'degree' of two-dimensionality of these vorticity

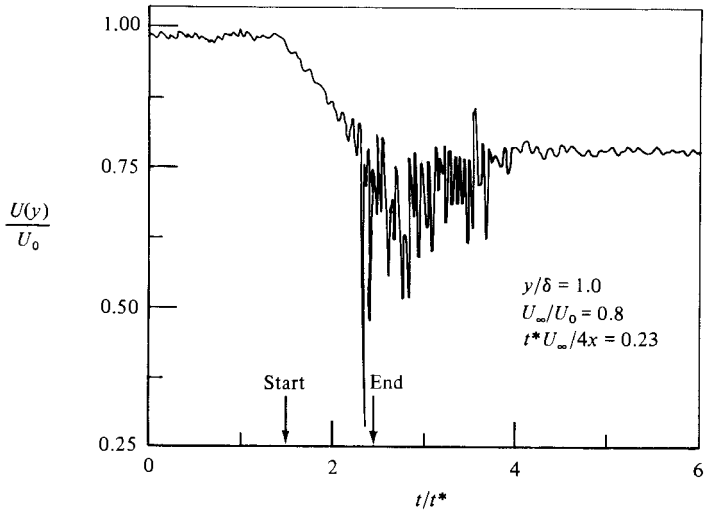

FIGURE 7. Longitudinal velocity away from the wall.

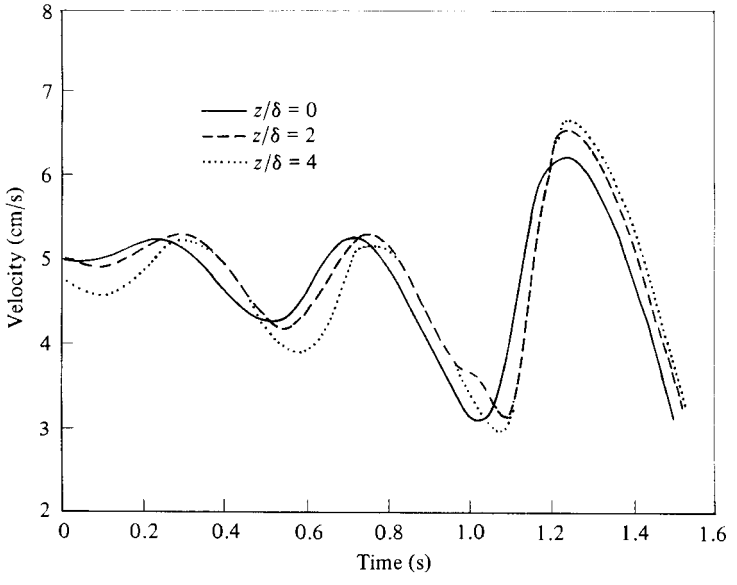

FIGURE 8. Spanwise variations of the instability waves.

waves, three hot-film probes were located at $y/\delta = 0.1$ at the same streamwise position $x/L = 0.8$, with a spanwise separation of two boundary-layer thicknesses. The plate was decelerated from 40 cm/s to 30 cm/s in 5 s. The streamwise-velocity signals from all three probes are plotted in figure 8. The waves are quite two-dimensional, although they have grown to relatively very large amplitude. Thus the development of a 'clean' two-dimensional wave field during the initial stages of the transition process on the decelerating flat plate contrasts with the mixed two-dimensional/three-dimensional field for the fixed-plate experiment (Anders & Blackwelder 1979).

The probe measurements are consistent with the qualitative visualization

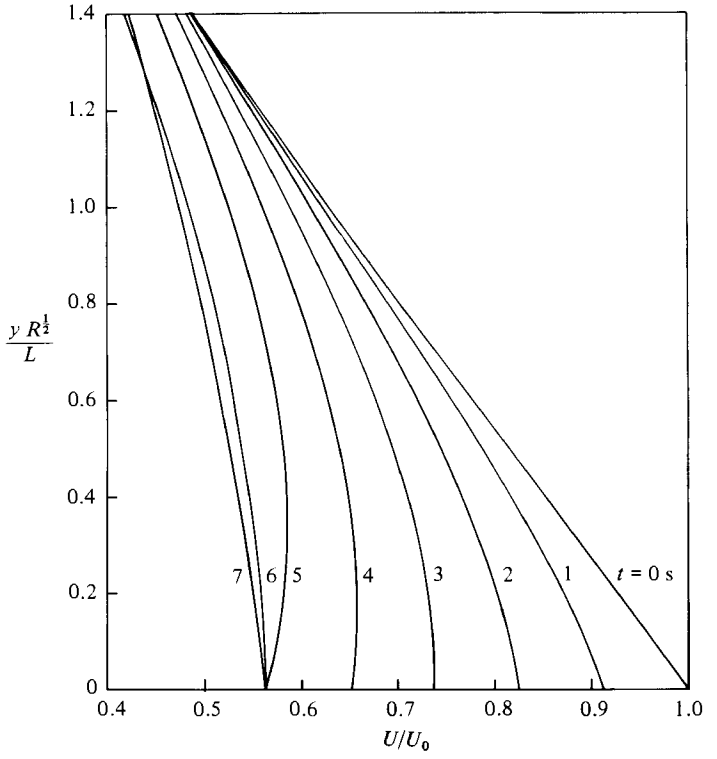

FIGURE 9. Typical solution of the unsteady boundary-layer equation; $U_0 = 40$ cm/s, $U_\infty = 22.5$ cm/s, $t^* = 5$ s.

experiments. The 'relaminarization' observed in the hot-film signal after the plate returns to a uniform speed does not show in the dye pictures, however, since the dye delineates the regions of the flow which have been marked by it, and at any instant of time it mainly gives information which is time-integrated over the history of the flow from the time of release of the dye.

4.3. *Numerical results*

The unsteady boundary-layer system (1) was solved by expanding the flow variables (dependence on y) in mapped Chebyshev-polynomial expansions, and discretizing x and t using Crank–Nicolson implicit space and time differencing. The code uses an unconditionally stable, spectral, accurate integration program for the solution of the time-dependent non-self-similar boundary-layer equations. The code is reasonably robust, having significant difficulty only in cases when the flow reverses so that the boundary-layer approximation is not valid.† This occurred for deceleration rates larger than 4 cm/s^2.

The resulting velocity profiles for a typical deceleration rate are presented in figure 9. Here the streamwise location was $x = 160$ cm, the initial and final speeds were 40 and 22.5 cm/s respectively and the deceleration rate was 3.5 cm/s^2. At $t = 0$ the velocity profile is of (inverted) Blasius type with the inflexion point at $y = 0$. The subsequent velocity profiles are inflexional, with the point of inflexion moving away

† Flow reversal changes the parabolic partial differential equation to an elliptic one requiring both inflow and outflow boundary conditions.

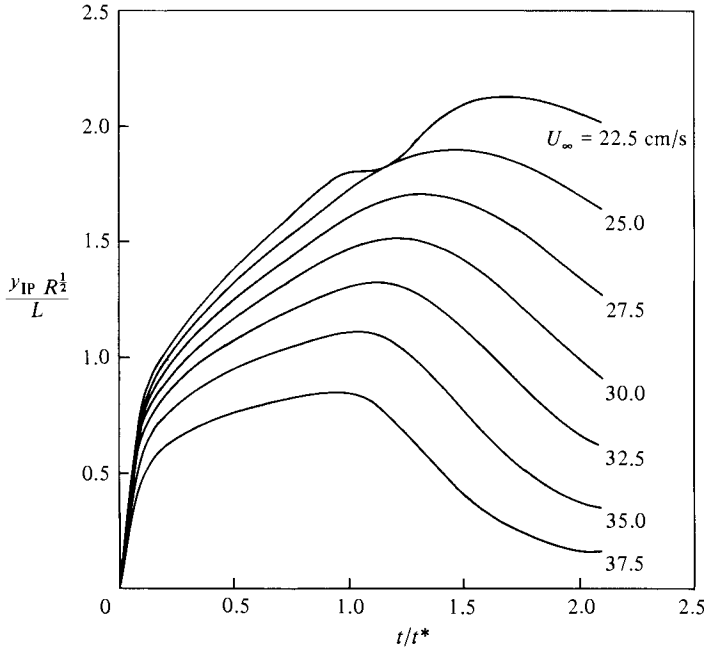

FIGURE 10. Migration of the inflexion point during deceleration; $U_0 = 40$ cm/s, $t^* = 5$ s.

from the wall on a viscous-diffusion timescale. At large times a new Blasius profile is established after the inflexional point returns back to the wall.

The unsteady boundary-layer equation was solved for a range of initial and boundary conditions comparable to the experimental runs. Since the solution is non-self-similar, it is obtained at selected streamwise locations. The migration of the inflexion point for seven different deceleration rates is shown in figure 10. The position $y_{IP}(t)$ of the inflexion point is normalized with the lengthscale $L/R^{\frac{1}{2}}$, and the time t is normalized with the deceleration time t^*. The initial speed was $U_0 = 40$ cm/s, and the plate was decelerated in a time $t^* = 5$ s to a final speed $U_\infty = 37.5$, 35.0, 32.5, 30.0, 27.5, 25.0 and 22.5 cm/s. The dip in the curve corresponding to a final speed $U_\infty = 22.5$ cm/s is an indication of the incipient breakdown of the numerical simulation as mentioned above. The inflexion point migrates farther from the wall for high deceleration rate. It reaches a particular position above the wall in a time that is inversely proportional to the deceleration rate. This is consistent with the experimental observation that transition occurs sooner for higher deceleration rates, provided that there is a 'most-dangerous' location above the wall for the inflexion point.

The flow field resulting from solving the unsteady boundary-layer equation was then subjected to stability analysis using the Orr–Sommerfeld equation applied to the instantaneous velocity profiles. The linear stability equation was solved using Chebyshev-polynomial spectral methods (Orszag 1971). As expected, the inflexional velocity profiles yielded lower critical Reynolds numbers and larger growth rates in the unstable region as compared with the Blasius profile. The neutral-stability curves during a typical deceleration are depicted in figure 11 (*a*), and enlarged in figure 11 (*b*). The plate was decelerated from an initial speed 40 cm/s to a final speed 30 cm/s in 5 s. At $t = 0$ the neutral stability curve for a Blasius profile resulted. As the plate decelerates, the inflexion point migrates away from the wall and the neutral-stability

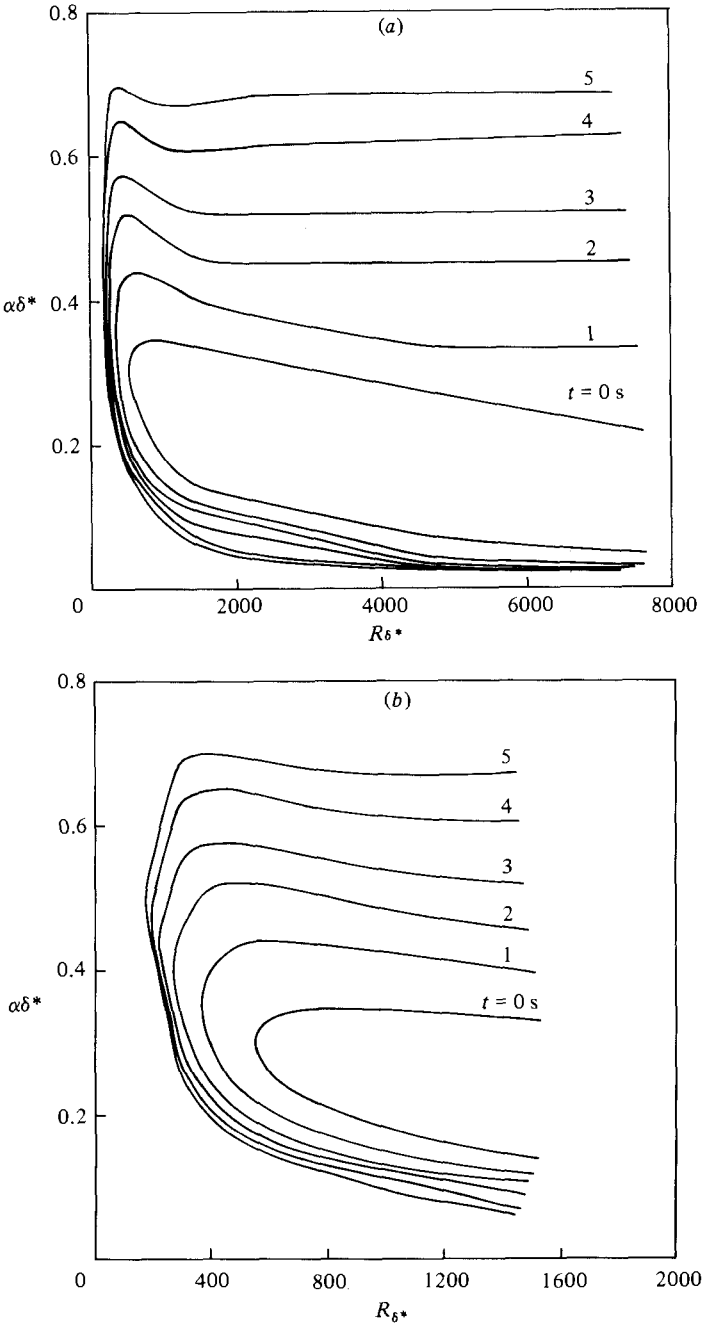

FIGURE 11. Neutral stability curves during deceleration; $U_0 = 40$ cm/s, $U_\infty = 30$ cm/s, $t^* = 5$ s.

curve moves toward the left, reaching its foremost left position at the end of the deceleration period ($t = 5$ s). Note that the inflexion point for this run reaches its maximum distance from the wall at $t = 6.25$ s (see figure 10). Finally, the inflexion point moves toward the wall and the neutral stability curve moves back toward the neutral curve of the Blasius profile. The unstable modes for the inflexional velocity

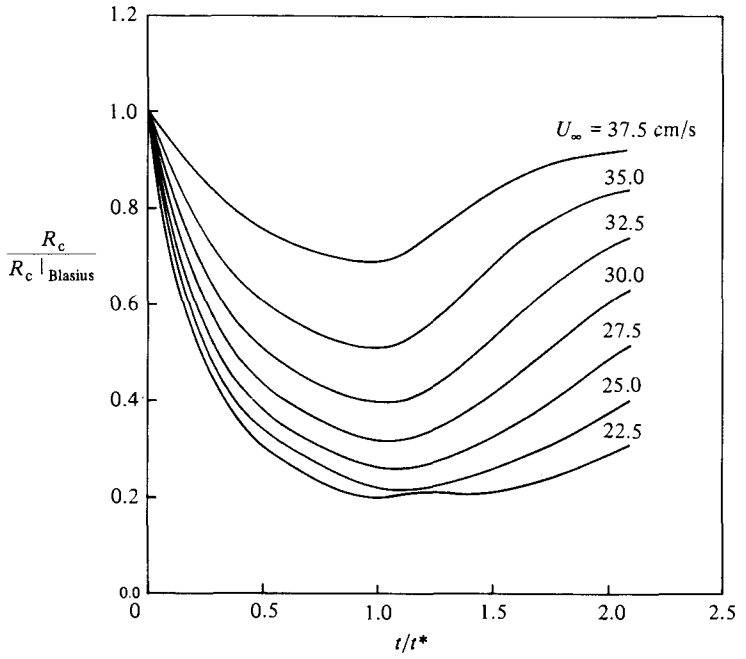

FIGURE 12. Plots of critical Reynolds number *vs.* time; $U_0 = 40$ cm/s, $t^* = 5$ s.

profiles tend to have larger wavenumbers (smaller wavelengths) as compared with the unstable modes for a Blasius velocity profile.

The critical Reynolds number for a particular velocity profile is the smallest value of Reynolds number for which an unstable eigenmode exists. The behaviour of the critical Reynolds number for seven different deceleration rates is shown in figure 12. The critical Reynolds number R_c is normalized with the critical Reynolds number for a Blasius velocity profile ($R_c|_{Blasius} = 520$), and the time t is normalized with the deceleration time t^*. The plate was decelerated from an initial speed $U_0 = 40$ cm/s to a final speed $U_\infty = 37.5$, 35.0, 32.5, 30.0, 27.5, 25.0 or 22.5 cm/s in a time $t^* = 5$ s. The critical Reynolds number decreases with time, then tends back to the Blasius value as the inflexion point migrates back toward the wall. The lowest critical Reynolds number decreases as the deceleration rate increases, and occurs at $t/t^* = 1$. For a deceleration rate of 3.5 cm/s^2, the lowest critical Reynolds number is about 20 % of the corresponding Blasius value.

The critical Reynolds number indicates qualitatively the 'degree' of instability for a particular experimental condition, where the actual Reynolds number usually far exceeds the critical one. For a certain decelerating boundary layer, the Reynolds number changes with time at a prescribed streamwise location on the plate. Of particular interest to the experiment is then to determine, at a particular location on the plate, the most-unstable mode at each instant of time. Vertical scans of the stability diagrams were conducted at the experimental Reynolds number at $x = 160$ cm, corresponding to a typical observation station. The results are depicted in figures 13–16.

The imaginary part of the eigenvalue ω_i indicates the exponential growth (or damping) of the disturbance amplitude. Figure 13 shows the growth rate ω_i versus wavelength $\lambda(\equiv 2\pi/\alpha)$ for the unstable modes as a plate is decelerated from 40 cm/s to 30 cm/s in 5 s. It is seen that, for each velocity profile, there exists a 'most-

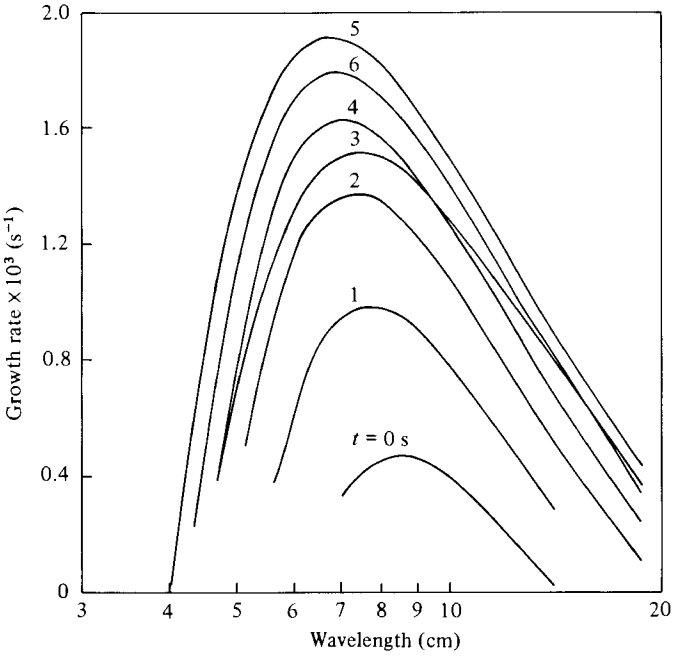

FIGURE 13. Plots of growth rate *vs.* wavelength for the unstable modes; $U_0 = 40$ cm/s, $U_\infty = 30$ cm/s, $t^* = 5$ s.

dangerous' wavelength corresponding to the maximum growth rate. As time increases, this most-dangerous wavelength decreases slightly. This is consistent with the experimental observation (§4.1) that the observed wavelength in the present decelerating-plate experiment is shorter than the Tollmein–Schlichting wave in a Blasius boundary layer. In particular, at $t = 5$ s, the most-dangerous wavelength is about 6.5 cm, whereas at $t = 0$ it is 8 cm. The computations were repeated for a plate decelerated from 40 cm/s to 25 cm/s and 35 cm/s in 5 s. The most dangerous wavelength at the end of the deceleration period varied in the range 5–7 cm, decreasing as the deceleration rate increased. This relative insensitivity of the lengthscale to changing the deceleration rate was observed in the flow-visualization experiments (§4.1).

Unlike the wavelength, the growth rate of the disturbance depends strongly on the deceleration rate. The maximum growth rate during deceleration for all three deceleration rates (1, 2 and 3 cm/s^2) is shown in figure 14. It increases as the deceleration takes place, reaching a maximum at the end of the deceleration period ($t = 5$ s), then declines moving back towards the Blasius value. At a particular time during the deceleration, the growth rate increases as the deceleration rate increases. At the end of the deceleration period, the maximum growth rate for a plate decelerated to a final speed $U_\infty = 25$, 30 and 35 cm/s is respectively about 5, 4 and 2 times that for a Blasius velocity profile.

The real part of the eigenvalue ω_r is proportional to the phase velocity of the two-dimensional disturbance $c_p (\equiv \omega_r/\alpha)$. Figure 15 shows the phase velocity versus wavelength for the unstable modes for different times during a deceleration from 40 cm/s to 30 cm/s in 5 s. For a particular wavelength, the phase velocity decreases as the plate is decelerated, reaching a minimum at the end of the deceleration period. The phase velocity for the most-amplified disturbance during deceleration is shown in figure 16 for three deceleration rates 1, 2 and 3 cm/s^2. Consistent with the

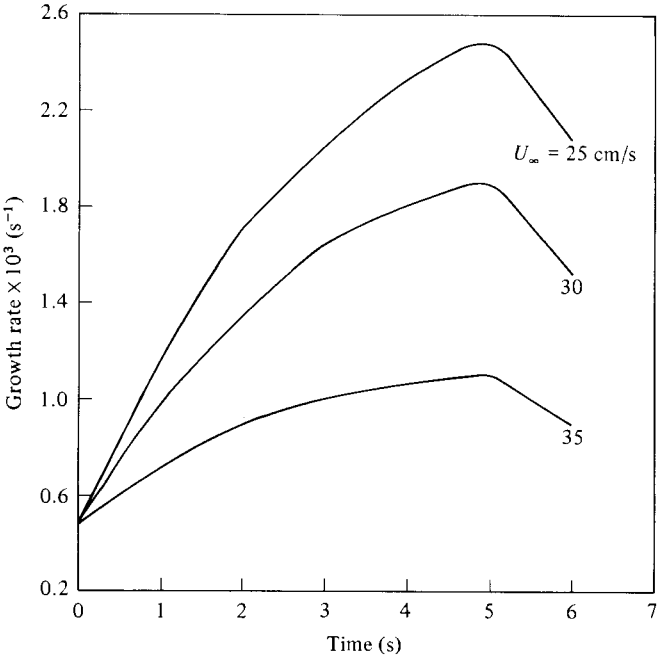

FIGURE 14. Maximum growth rate during deceleration; $U_0 = 40$ cm/s, $t^* = 5$ s.

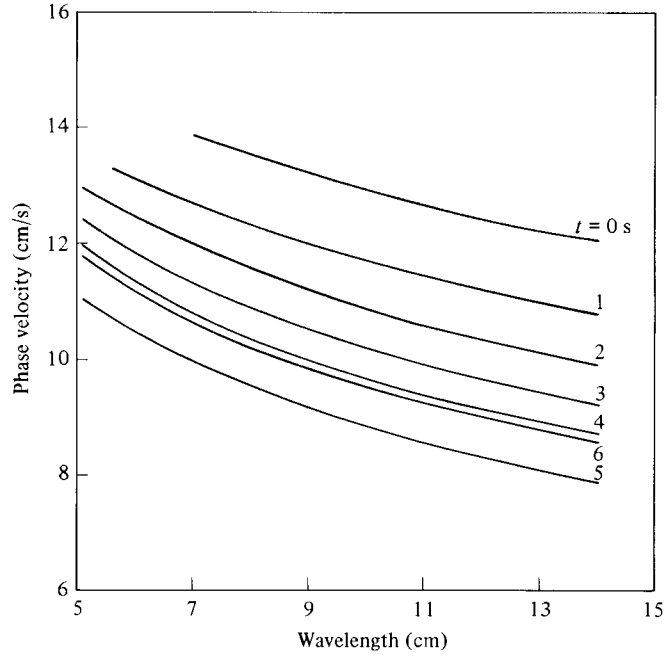

FIGURE 15. Plots of phase velocity *vs.* wavelength for the unstable modes; $U_0 = 40$ cm/s, $U_\infty = 30$ cm/s, $t^* = 5$ s.

flow-visualization results, the phase velocity for the inflexional velocity profiles is less than that for the Blasius boundary layer. For a plate decelerated to a final speed 25, 30 and 35 cm/s and at the end of the deceleration period ($t = 5$ s), the phase velocity for the most-amplified disturbance is respectively 63, 74 and 87 % of that for a Blasius velocity profile.

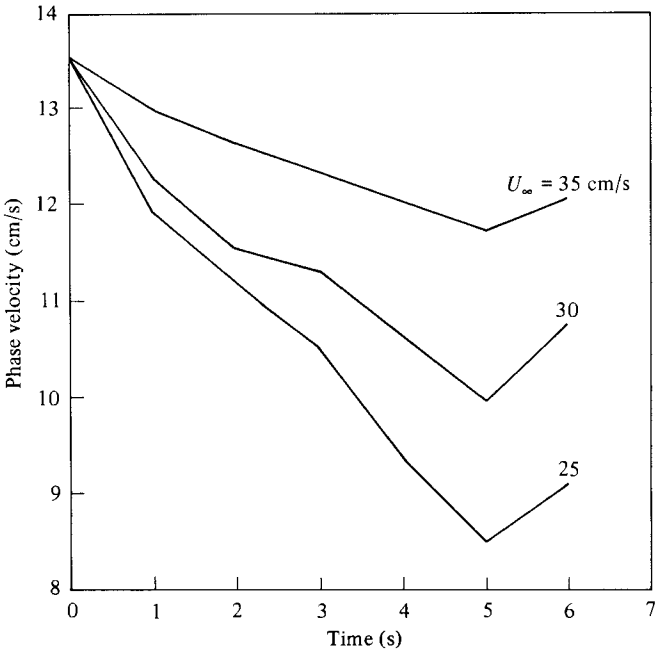

FIGURE 16. Phase velocity of most-amplified disturbance during deceleration; $U_0 = 40$ cm/s, $t^* = 5$ s.

The full decelerating boundary layer of (2) grows spatially in x and evolves in time t. In the above analysis we have assumed that the stability characteristics can be determined from velocity profiles that are locally parallel and quasi-steady. The locally parallel assumption has been discussed thoroughly by Saric & Nayfeh (1975). We now discuss the quasi-steady assumption.

For $t \to 0$ and $t \to \infty$, the local velocity profiles are of Blasius type so that the upper and lower branches of the neutral curves close as $R_{\delta^*} \to \infty$, consistent with these profiles being stable by inviscid theory. Thus, for *fixed* $\alpha\delta^*$ consider raising R_{δ^*} from zero. The flow is stable below the neutral curve and is unstable inside the stability loop. The disturbances attain (numerically small) maximum growth rates inside the loop but for R_{δ^*} large enough the flow is again stable. On the other hand, local velocity profiles corresponding to intermediate times t have inflexion points. Their quasi-steady neutral curves, shown in figure 11, are open to infinity since these profiles are unstable by inviscid theory. We again consider raising R_{δ^*} for $\alpha\delta^*$ *fixed*. The flow is stable below the neutral curve and becomes unstable inside the stability loop. However, the growth rates of the disturbances increase continuously as $R_{\delta^*} \to \infty$, the inviscid values being substantial. The quasi-steady theory should correctly describe this region since the growth rates can be large compared with the rate of change of the basic unsteady boundary layer. In particular this theory should give the structure of the upper and lower branches. As R_{δ^*} is lowered, the description of these branches should begin to deteriorate, the poorest approximation occurring at the neutral curve where the predicted growth rates are zero (Davis 1976). The growth rates shown in figure 13 correspond to a vertical scan of figure 11 in that they are taken at *fixed* R_{δ^*}. Since R_{δ^*} is only slightly supercritical, the maximum growth rates shown are numerically small (though still much larger than those of Blasius layers). The rationale of the present work lies in the observation that the quasi-steady theory should be good for

large R_{δ^*} and *may* be qualitatively useful at smaller R_{δ^*}. The fact that the predictions of the theory and the observations of the experiment are in good qualitative agreement supports our description of the mechanics of the early part of the transition process for the decelerating boundary layer.

5. Concluding remarks

The stability of the decelerating laminar boundary layer was investigated experimentally and numerically. The experiments were conducted in an 18 m towing tank, using a flat-plate geometry. Flow-visualization and probe-measurement experiments were conducted. The flow field was visualized using fluorescent dyes and sheets of argon laser light. The instantaneous longitudinal velocity was measured using an array of miniature hot-film probes.

A Blasius boundary layer subjected to uniform deceleration underwent a well-defined route to complete transition. The visualization experiments revealed the onset of two-dimensional waves that appeared after the deceleration had started, three-dimensionality was then apparent and led to the formation of hairpin vortices that lifted away from the wall and burst into turbulence.

The formation and growth of the vorticity waves in the decelerating laminar boundary layer were also observed using hot-film probes. The probes were moved with the plate, and indicated high-speed (relative to the plate) fluid coming from the outer parts of the ambient fluid towards the wall region. The probes also indicated a return to the laminar state after the deceleration ceased. The probe measurements indicated the 'degree' of two-dimensionality of the vorticity waves observed in the decelerating-plate experiment. The waves were truly two-dimensional; and that suggests the study of their instability in order to determine the mechanism and characteristics of the development of three-dimensionality. If there is a well-defined transition from laminar two-dimensional waves to laminar three-dimensional waves through an instability process, one has identified a major link in the transition process.

The unsteady boundary-layer equations were solved numerically to generate instantaneous velocity profiles for a range of boundary and initial conditions. The resulting velocity profiles were inflexional, with the inflexion point initially at the wall, moving upward on a diffusion timescale and finally going back to the wall. The unsteady flow field was subjected to stability analysis using the Orr–Sommerfeld equation applied to the instantaneous, locally parallel velocity fields. The generalized matrix eigenvalue problem was solved using Chebyshev-polynomial spectral methods (QR method).

For profiles at a given station $x = x_0$, the stability calculation shows that the inflexional case has smaller wavelength, smaller phase speed and lower critical Reynolds number than the corresponding Blasius profile. All these trends are consistent with the observations and measurements made. This gives us confidence that the mechanics of the initial instability is well understood. However, the observed appearance of two-dimensional instabilities (say in a 5 s deceleration run) occurs earlier in the deceleration history (e.g. at $t \approx 2$ s) than one would predict from the 'most-dangerous' profile obtained from the stability calculations (for which one would have $t \approx 5$ s). In this calculation we used profiles consistent with the measurement station at $x = x_0$. Although one cannot rule out nonlinear effects, the more likely reason for such 'earlier' instability is the non-self-similarity of the decelerating boundary layer. Self-similarity of the flow implies that profiles at all stations are 'equivalent' in terms of stability characteristics. When the flow is not self-similar,

the profiles at different stations are not equivalent, each profile needs to be examined separately and the 'most-dangerous' station selected. The early appearance of instabilities in the present observations suggests that there are more-unstable profiles at neighbouring stations whose instabilities propagate to the observation station and are seen before the local profile itself becomes unstable.

In summary then we have both flow visualization and point measurements for the instability and transition processes of flows on decelerating plates. We have obtained theoretical descriptions of the unsteady boundary layer and its instability to two-dimensional laminar waves. These give a consistent picture of the early steps of the transition process.

The work on the stability of decelerating *laminar* boundary layers is a step toward understanding the more complicated problem of the effects of acceleration or deceleration on *turbulent* boundary layers. This problem has obvious relevance in accelerating or decelerating vehicles, vehicles experiencing turn and other manoeuvres, rotating propellers, and many other practical situations.

On a more basic side, the deceleration experiment offers a convenient way to modulate laminar and turbulent boundary layers; in a way analogous to using pressure gradient, heating or roughness to help determine the exact nature of the apparent analogies between the different transition events in a laminar boundary layer and the intermittent events that characterize fully developed turbulent boundary layers; namely the bursting cycle.

This work is sponsored by the U.S. Air Force Office of Scientific Research, under Contract F49620-78-C-0062, and NASA-Ames Research Center, under Contract NAS2-10997. The continuous support of the program monitors, Captain M. S. Francis and Dr A. Leonard, is greatly appreciated. The authors would like to acknowledge the valuable help of R. F. Blackwelder, G. Chapman, H. Huynh, M. V. Morkovin, J. J. Riley and R. Srnsky.

REFERENCES

ANDERS, J. B. & BLACKWELDER, R. F. 1979 Longitudinal vortices in a transitioning boundary layer. In *Laminar–Turbulent Transition* (ed. R. Eppler & H. Fasel), p. 110. Springer.

CRAIK, A. D. D. 1971 Non-linear resonant instability in boundary layers. *J. Fluid Mech.* **50**, 393.

CRAIK, A. D. D. 1980 Nonlinear evolution and breakdown in unstable boundary layers. *J. Fluid Mech.* **99**, 247.

DAVIS, S. H. 1976 The stability of time-periodic flows. *Ann. Rev. Fluid Mech.* **8**, 57.

DAVIS, S. H. & GAD-EL-HAK, M. 1981 Transition in decelerating boundary layers. *Bull. Am. Phys. Soc.* **26**, 1251.

DRAZIN, P. & REID, W. 1981 *Hydrodynamic Stability.* Cambridge University Press.

FALES, E. N. 1955 A new laboratory technique for investigation of the origin of fluid turbulence. *J. Franklin Inst.* **259**, 491.

FOX, L. & PARKER, I. B. 1968 *Chebyshev Polynomials in Numerical Analysis.* Oxford University Press.

GAD-EL-HAK, M., BLACKWELDER, R. F. & RILEY, J. J. 1979 A visual study of the growth and entrainment of turbulent spots. In *Laminar–Turbulent Transition* (ed. R. Eppler & H. Fasel), p. 297. Springer.

GAD-EL-HAK, M., BLACKWELDER, R. F. & RILEY, J. J. 1981 On the growth of turbulent regions in laminar boundary layers. *J. Fluid Mech.* **110**, 73.

HEGARTY, J. C. 1958 Investigation of transition caused by the stopping of a flat plate. *AFOSR* TN58-627.

JORDINSON, R. 1970 The flat plate boundary layer. Part 1. Numerical integration of the Orr–Sommerfeld equation. *J. Fluid Mech.* **43**, 801.

KLEBANOFF, P. S., TIDSTROM, K. D. & SARGENT, L. M. 1962 The three-dimensional nature of boundary layer instability. *J. Fluid Mech.* **12**, 1.

LIEPMANN, H. W., BROWN, G. L. & NOSENCHUCK, D. M. 1982 Control of laminar-instability waves using a new technique. *J. Fluid Mech.* **118**, p. 187.

LIN, C. C. 1955 *The Theory of Hydrodynamic Stability*. Cambridge University Press.

NAYFEH, A. H. & BOZATLI, A. N. 1979 Nonlinear wave interactions in boundary layers. *AIAA 12th Fluid & Plasma Dyn. Conf., Williamsburg, Paper* 79–1496.

ORSZAG, S. A. 1971 Accurate solution of the Orr–Sommerfeld stability equation. *J. Fluid Mech.* **50**, 689.

ORSZAG, S. A. & PATERA, A. T. 1983 Secondary instability of wall-bounded shear flows. *J. Fluid Mech.* **128**, 347.

PERRY, A. E., LIM, T. T. & TEH, E. W. 1981 A visual study of turbulent spots. *J. Fluid Mech.* **104**, 387.

ROSENHEAD, L. (ed.) 1963 *Laminar Boundary Layers*. Clarendon.

SARIC, W. S. & NAYFEH, A. H. 1975 Non-parallel stability of boundary-layer flows. *Phys. Fluids* **18**, 945.

SCHLICHTING, H. 1968 *Boundary Layer Theory*. McGraw-Hill.

SQUIRE, H. B. 1933 On the stability of three-dimensional disturbances of viscous flow between parallel walls. *Proc. R. Soc. Lond.* A **142**, 621.

STEWARTSON, K. 1951 On the impulsive motion of a flat plate in a viscous fluid. *Q. J. Mech. Appl. Maths* **4**, 182.

STUART, J. T. 1965 The production of intense shear layers by vortex stretching and convection. *AGARD Rep.* 514.